Available online at www.sciencedirect.com
ScienceDirect
Journal of Applied Geophysics 62 (2007) 215–233
JOURNAL OF APPLIED GEOPHYSICS
www.elsevier.com/locate/jappgeo

The application of shallow seismic techniques in the study of active faults: The Atalanti normal fault, central Greece

V.K. Karastathis [a,*], A. Ganas [a], J. Makris [b], J. Papoulia [c], P. Dafnis [d], E. Gerolymatou [a], G. Drakatos [a]

[a] National Observatory of Athens, Institute of Geodynamics, PO Box 20048, 118 10 Athens Greece
[b] GEOPRO GmbH, St. Annenufer 2, 20457 Hamburg, Germany
[c] Hellenic Centre of Marine Research, Institute of Oceanography, P.O. Box 712, 19013 Anavissos, Attiki, Greece
[d] Geoskopio ATE, Emm. Papadaki 19, N. Herakleio, 14121 Athens, Greece

Received 24 January 2006; accepted 6 November 2006

Abstract

Shallow seismic surveys can constitute a useful tool in actively deforming regions by yielding precise information on the location of active faults, their geometry and cumulative displacement. Since the structures in these regions are rarely flat but always with sharp dips, 3D effects and side reflections can influence the results, thus the interpretation must be combined with geomorphological and geological data.

The application of shallow seismic techniques in the hanging wall area of the Atalanti normal fault, central Greece, provided new data on hanging wall deformation, the amount of crustal extension and the long-term slip distribution along the fault.

Keywords: Fault; Atalanti; Shallow seismic; MASW; Crustal extension; Central Greece

1. Introduction

In many areas crosscut by active faults the application of deep seismic methods is difficult because of rapid urbanization, heavy agriculture etc. In such areas the application of shallow seismics can provide crucial information on deformation patterns in the hanging wall area and help the study of the active faults.

The Atalanti Fault is a large, active normal fault in central Greece with an average strike of N290°E and dip to the north-east (Fig. 1; Rondoyianni-Tsiambaou, 1984; Ambraseys and Jackson, 1990; Ganas et al., 1998; Pantosti et al., 2001, 2004). The fault is a Late Pliocene–Quaternary structure and accommodates crustal extension across the Gulf of Evia rift (Fig. 1). The fault starts a few kilometres to the north-west of the town of Atalanti and terminates near the town of Larymna, about 34 km to the south-east (Ganas et al., 1998; Fig. 1). The fault ruptured during the 1894 earthquake sequence when two main shocks occurred 15–20 km apart with a time difference of one week (April 20 and 27, 1894; Skouphos, 1894; Ambraseys and Jackson, 1990). The earthquakes killed more than 250 people, injured several hundred and shattered thousands of houses thus creating a legendary event in modern Greek history (Mitsopoulos, 1895).

* Corresponding author. Fax: +30 210 3490180.
E-mail address: Karastathis@gein.noa.gr (V.K. Karastathis).

0926-9851/$ - see front matter © 2006 Elsevier B.V. All rights reserved.
doi:10.1016/j.jappgeo.2006.11.004

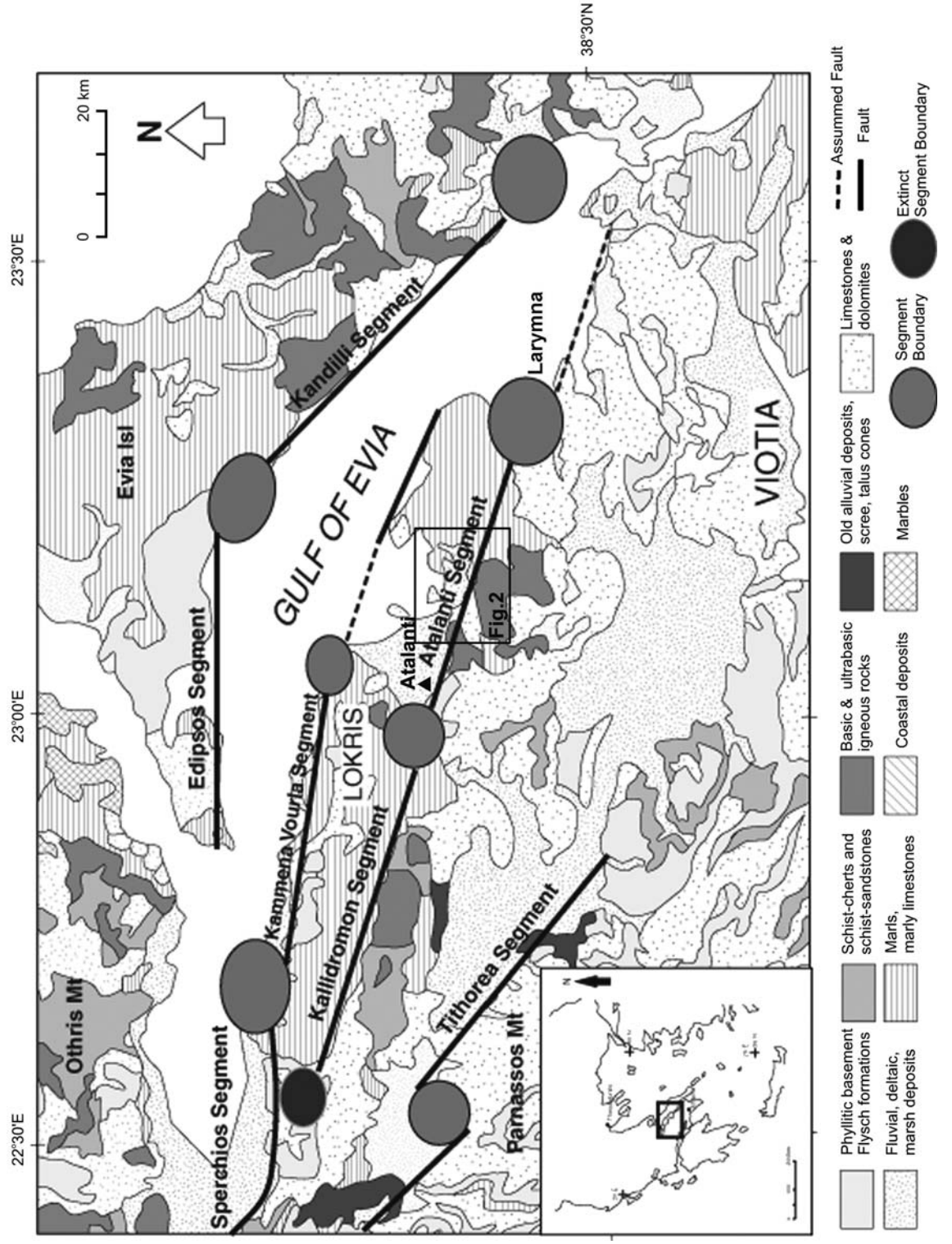

Fig. 1. Map of the province of Lokris that was totally ruined after the two strong earthquakes in April 1894. The origin of the double shock was attributed to the activation of the Atalanti Fault. Modified after Ganas and Papoulia (2000).

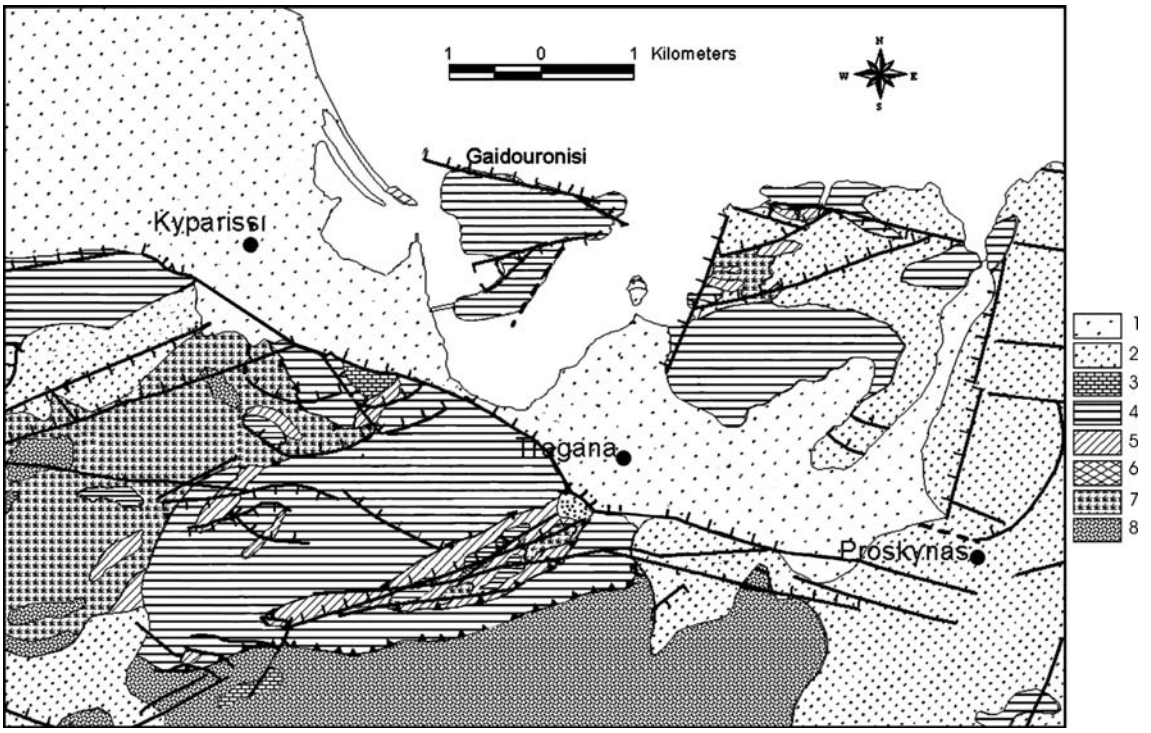

Fig. 2. The geological map of the investigated area. The formations numbered are: 1. Quaternary undivided 2. Neogene undivided 3. Upper Cretaceous transgressive limestone 4. Middle and lower Jurassic Limestone 5. Middle to lower Jurassic shales–cherts 6. Upper Middle Triassic Dolomite 7. Peridotite 8. Diabas–Dolerite. Lines with ticks indicate normal faults. Lines with teeth indicate thrust faults. Modified after IGME (1965).

During the last fifteen years the active fault zone of Atalanti has strongly attracted the interest of the scientific community (Ambraseys and Jackson, 1990; Ganas et al., 1998; Buck and Stewart, 2000; Cundy et al., 2000; Pantosti et al., 2001, 2004; Papaioannou et al., 2004; Pavlides et al., 2004) due to the concern of the public, who consider it as one of the most serious natural threats in Greece. Although the seismicity $M>5$, after the 1894 events, was almost negligible, the Atalanti fault area is very popular with seismologists as many projects have been conducted in the area, many papers have been published and many technical reports have been submitted to relevant governmental organisations. Most of past studies in the area were based on geological–geomorphological observations and historical references and less on seismological or geophysical experiments. Their results were frequently contrary to each other regarding the fault's length and characteristics, the epicentres of the 1894 earthquakes and the seismic hazard of the area. The most recent studies (Pavlides et al., 2004) consider the fault zone to be noncontinuous, but divided into five segments, with very long return periods in time, one per 1000 yrs or more, thereby downgrading the perceived seismic hazard.

The central part of the fault zone, between Kyparissi and the Tragana village (Fig. 2) was the area with the most intensive phenomena during the large earthquakes of 20/4/1894 (Ms 6.4) and 27/4/1894 (Ms 6.9).[1] In particular, subsidence was observed along a major part of the coastal zone as well as extensive liquefactions (Skouphos, 1894; Ambraseys and Jackson, 1990). The subsidence also caused the separation of the "Gaidouronisi" peninsula (see Fig. 2) from the coast thereby creating the so-called island.

The present study aims to determine the shallow structure of this area. The objectives include the description of the Tragana basin, the location of the faults and their geometry, the stratigraphy of the hanging wall as well as the detection of the aquifers at shallow depths.

In addition, knowledge of the geometric and kinematic characteristics of the Atalanti fault as well as the structure of the Tragana basin are very useful in estimating the model peak ground acceleration and the deformation pattern for the 1894 earthquakes and to correlate it with the macroseismic observations i.e.

[1] The magnitudes given are according to Ambraseys and Jackson, 1990.

subsidence, liquefactions etc. However, this paper will focus only on the geophysical investigations of the main characteristics of the fault and the bedrock's structure.

2. Geological setting

The study area lies in the North Evoikos Gulf, which is a tectonic graben formed in Late Pliocene–Early Quaternary period by normal faults striking NW–SE (Roberts and Jackson, 1991; Pavlides et al., 2004). The bedrock consists of alpine rocks of Subpelagonic zone, while the overlying sediments are Neogene and Quaternary.

The geological map of the study area is depicted in Fig. 2. Placed in chronological order, the bedrock's tectonostratigraphic column contains: 1. Quaternary sediments — sands, gravels, clays and talus 2. Neogene undivided — marls, clays, gravels, sandstones, conglomerates, and marly limestone 3. Upper Cretaceous transgressive limestone — thin plated marly limestones with radiolites 4. Middle and lower Jurassic — limestone often oolitic in the upper horizons. 5 Middle to lower Jurassic shales–cherts 6. Upper Middle Triassic — compact dolomites 7. Peridotite, dunite, pyroxeno–peridotite 8. Diabase, dolerite (IGME, 1965).

The April 27, 1894 earthquake ruptured the pre-rift/syn-rift contact in the region of Atalanti–Martinon (Skouphos, 1894). The pre-rift rocks are: a) hard, resistant carbonates occurring mainly near Kyparissi and Larymna, b) an ophiolitic complex near Kyparissi and Proskynas, and c) a volcano–sedimentary unit near Atalanti which lies at the base of the Sub-Pelagonian zone of the Hellenides. The syn-rift rocks are Pliocene and Pleistocene sediments. The Pliocene comprises sands, clays, yellow marls, and well-sorted pebbles, formed in a fluvio-lacustrine environment. The Pleistocene sediments are alluvial fan deposits, talus cones and scree, fluvial conglomerates and breccias. The sedimentary basin is developed more to the north-west (Ganas et al., 1998) and fault throws are diminishing gradually to the south-east. This asymmetry in fault growth may reflect a complexity in earthquake occurrence along this fault.

3. Data acquisition

The geophysical survey was organised in a way to give information about:

1. the main structural characteristics of the Atalanti fault at the site of the investigation
2. the possible existence of other faults in the area
3. the morphology of the basin formed by active faults
4. the tectonic regime which could justify the large subsidence of the coast
5. the local hydrogeological conditions that allowed the liquefactions of 1894.

Seismic wide-angle reflection and refraction profiles were conducted at 17 sites in total, in order to investigate the whole area in detail (Fig. 3). The long seismic profile AA' was about 5 km long, perpendicular to the coast and half of it was placed offshore. Its direction and length were chosen in a way to detect the Atalanti fault and also to give information for the basin of Tragana. Thirty-six seismic recording systems SEDIS III, developed in GEOPRO, Hamburg (Makris and Moeller, 1990), with 6 channels per instrument, were deployed to acquire the data of the long profile. The positions of the land seismic sources and ocean bottom seismographs (OBSs) are indicated on the seismic line AA' in Fig. 3, but those of the 125 geophones, installed with spacing of 20 m and the 280 airgun shots fired about every 10 m are not depicted. Since the major part of the inland profile was located in urban environment, we used a large accelerated dropping weight instead of explosives which are typically used in such long profiles. In the offshore part we used an airgun as the seismic source. In the land seismic recording the noise was considerably higher because of the existence of the National Highway across the profile with continuous traffic. However, the signal was of adequate quality, even at offsets of 1 km.

In the other 16 seismic profiles, we recorded both P and S refracted and reflected seismic waves using the respective seismic sources. We also used, in most cases, Multi-channel Analysis of Surface Waves (MASW) (Park et al., 1999) in order to map the s-wave velocity. The locations of the profiles are shown in Fig. 3. The short seismic profiles were carried out with a portable seismograph EG&G Geometrics and 24 triaxial geophones of 4.5 Hz. The length of the various layouts varied from a maximum of 288 m to a minimum of 72 m. By modelling the reflection arrivals, some of these profiles succeeded in estimating the depth of the bedrock, even at depths of hundreds of metres. However the main target of the small profiles was the quality evaluation of the soils and the detection of the shallow aquifers.

4. Data processing

The data processing was mainly based on seismic refraction tomography techniques, as well as inverse traveltime modelling of the refracted and reflected

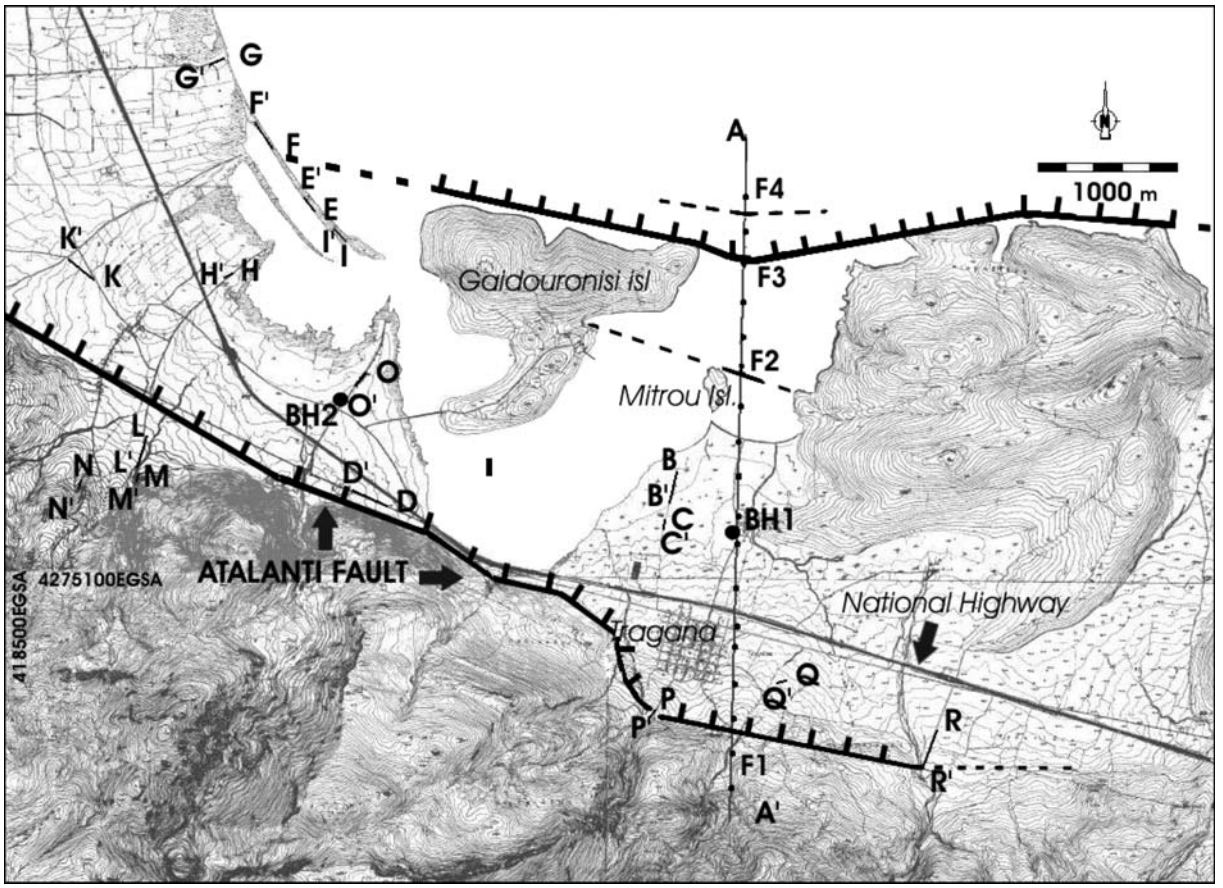

Fig. 3. Map with the positions of the seismic surveys (4 m contours from Hellenic Army Geographical Service 1:5000 map sheets).

seismic body waves. Although the seismic refraction modelling and tomography are standard methods in shallow depth applications, modelling and tomography of the reflection arrivals are still quite unusual at these investigation depths, and few applications have been reported (Ditmar et al., 1999; Morozov and Levander, 2002). The main reason is the difficulty in recognising the reflection signal at the shallow depth conditions and moreover identifying the outset of its wavelet. In fact at the short offsets the signal is highly interfered with the ground-roll and airwave noise. In addition, the first reflectors are usually hindered behind the refraction first arrivals. Sometimes it is even possible to see the multiple energy of an early arrival reflection without clearly seeing the primary event. Problems are also introduced by the non-spiking shape of the pulse. Although the generated pulse of an impulsive source usually has minimum phase, the reflection signal can have a different phase so event identification needs to be done with great care. Deconvolution is usually not very helpful when applied to common-shot records of shallow depth data since it enhances the high frequency noise and therefore degrades the overall quality of the seismic data. In general, the filters applied to the record, before the identification process, must be implemented with special care in order not to distort the signal. Selecting the reflection arrivals is best done on the raw data after a minimum processing i.e. bandpass filtering.

The implemented inverse modelling technique was that of Zelt and Smith (1992). The inversion of seismic traveltimes accomplished the simultaneous determination of the 2-D velocity and interface structure, using all the possible phases of the seismic waves. In particular, in this method we took into account reflections, refractions, multiple reflections as well as mode converted phases. The method and its advantages over the classical forward modelling are presented in detail by Zelt and Smith (1992), and some additional features on the program are presented by Zelt and Forsyth (1994). The algorithm uses a forward traveltime modelling with ray-tracing to calculate the arrival times and an iterative inversion technique to adjust the

velocity model. The velocity model parameterisation is based on the consideration of velocity and boundary nodes (Fig. 4). The number and position of velocity and boundary nodes can be adapted to the shot-receiver geometry, the ray coverage and the complexity of the near-surface. The velocity field in a layer results from linear relations that take into account the positions of the nodes and the boundaries. The values of velocity and boundary nodes are updated simultaneously using successive application of a ray-tracing and damped least-squares inversion algorithm.

The seismic refraction tomography was based on a ray-tracing modelling algorithm with a simultaneous iterative reconstruction technique algorithm for inversion (Hayashi and Takahashi, 1997). The velocity model was constructed by many thin layers composed of quadrangle cells with uniform velocity value. The first arrival traveltimes and ray paths were calculated by the ray tracing method based on Huygens' principle. The algorithm calculates the fastest ray connecting nodes defined on the boundaries of the cells (Fig. 5).

The Multi-channel Analysis of Surface Waves (MASW) (Park et al., 1999; Xia et al., 1999; Lin et al., 2004) was also implemented in many survey lines at the investigation area in order to acquire the s-wave velocity model. The method is mainly based on the property of the surface wave dispersion, i.e. the change of the phase velocity with frequency. The dispersion curve (phase velocity vs frequency) is derived by a variety of techniques (McMechan and Yedlin, 1981; Gabriels et al., 1987; Park et al., 1999). Finally, an inversion technique is applied in order to estimate the proper s-wave velocity model. The inversion uses the measured dispersion curve as reference and by iterative inverse modelling constructs the velocity model that produces a similar curve.

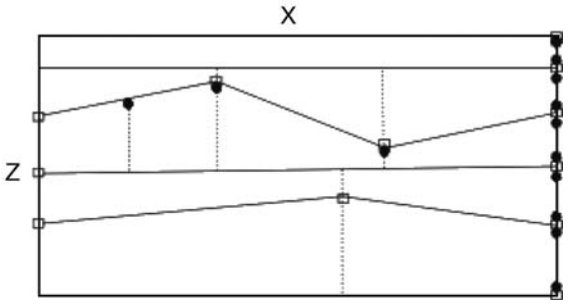

Fig. 4. Example of the parameterisation of the velocity model in the inverse modelling (Zelt and Smith, 1992). The squares represent the boundary nodes and the circles the velocity ones. In the ray-tracing stage the model is automatically divided into trapezoidal blocks. The layers which have one velocity node at their top and one at their bottom are laterally homogeneous.

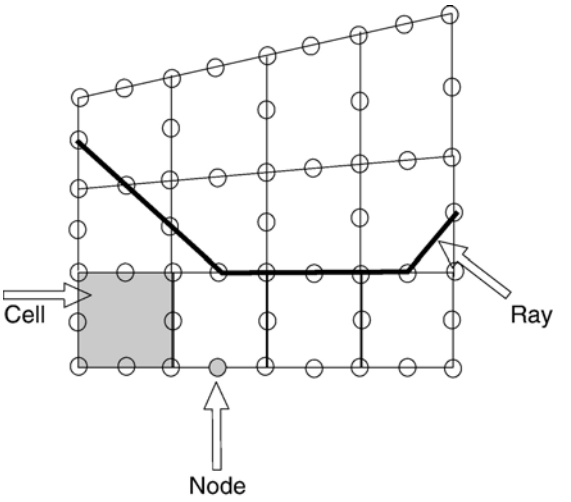

Fig. 5. The velocity model in the refraction tomography.

5. Results

5.1. Line AA′

We begin by describing the results of the long profile AA′ , which detected the Atalanti Fault and described its main structural characteristics at shallow depths. The seismic refraction tomography resulted in the cross-section shown in Fig. 6a. The offset axis has a starting point on the Tragana coast, so the negative offsets are located to the sea and the positive to the land. The velocity model between −180 and 0 m is omitted from the presentation since the depth of the waters was too shallow for the airgun shooting, and therefore the coverage could not give reliable results for this part. There was excellent fitting between the observed and the calculated traveltimes. The rocky formations have values over 3–3.5 km/s. In the lower part the result of the inverse traveltime modelling is given.

Fig. 6b depicts the result of the inverse modelling based on the ray-tracing technique. At the land section, three main geological formations can be considered, one at the surface with low seismic velocity values (up to 1 km/s), one in the middle with velocity values up to 2.2 km/s and finally one with high velocity up to 4.4 km/s. The three formations must represent a) the soft surface weathered material, b) sediments of sand and gravel with clay, and marls c) the limestone bedrock. At the offshore part, the first layer is water, the second with seismic velocity of about 2.2 km/s is a

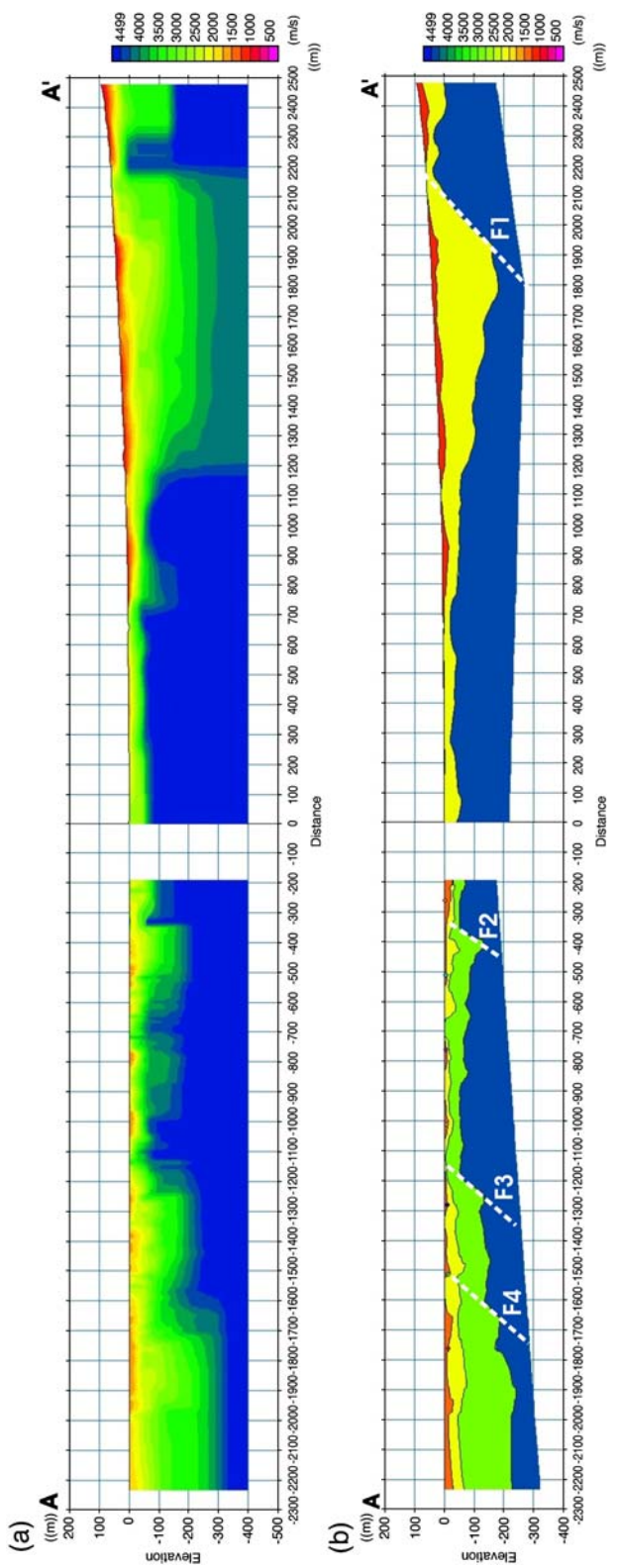

Fig. 6. (a) The refraction tomography profile of the AA'. (b) The inverse modelling results of the AA' profile. The zero point of the horizontal axis of distance is located at the coast. The negative and positive values are located at the marine and the land parts respectively.

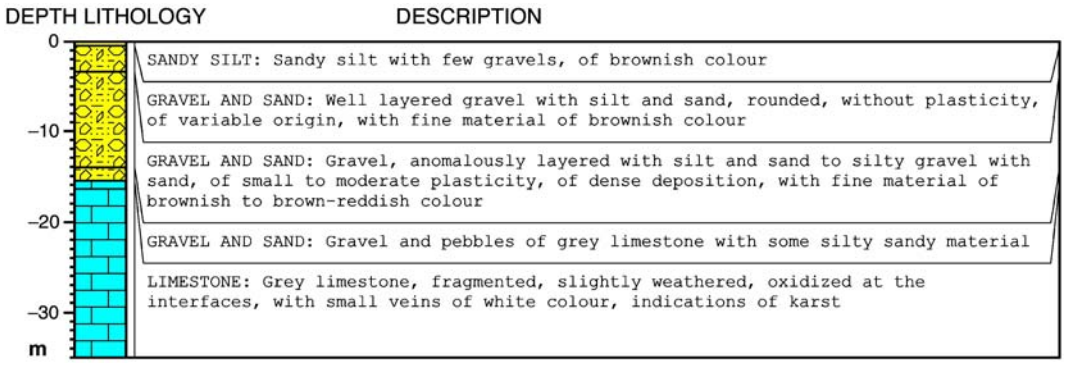

Fig. 7. The results of the drilling carried out at a distance of about 650 m from the coast, site BH1 (see Fig. 3).

sedimentary layer of sand and clay, the third, with velocity up to 3.0 km/s, is probably marly limestone and the bottom layer of seismic velocity 4.4 km/s is the limestone bedrock.

The results of the land profile were confirmed by the borehole BH1 (see Fig. 3 for the location) drilled at a distance of about 650 m from the coast. The geological interpretation of the borehole's core samples is given in Fig. 7.

The normal fault of Atalanti is obvious in the modelling section (Fig. 6b, fault F1) from the steep slope of the bedrock at a distance between 1.9 and 2.2 km from the coastline. The apparent dip of the fault seems to be about 45° and the throw is up to 200 m.

The surface expression of the fault F1 coincides with the surface rapture trace after the great earthquake of 1894. The trace is known from historical references (Skouphos, 1894). Our geophysical survey has imaged the bedrock interface in detail. The bedrock is rising from the basin depocentre to the coast with an apparent slope up to 10°.

5.2. Lines BB', CC'

The BB' and CC' lines throw more light onto the study of the area north of Tragana (between the coast and the National Highway). The positions of these two profiles are located at the western side of the long profile and are shown in Fig. 3. At this site, the earthquakes of 1894 caused extensive liquefactions and subsidence of the coastal zone.

The BB' 240 m long profile, obtained with the accelerated dropping weight, gave a clear picture of a strong reflector at a depth varying from 60 to 80 m (Fig. 8a) that can be attributed to the bedrock. In Fig. 8b an example of the reflection recording is given. At the shallower depths, where the reflections had not much resolution, refracted arrivals also found another possible horizon at about 35 m depth. Additionally, the Multi-channel Analysis of Surface Waves method (MASW) showed that this layer is quite consolidated.

The seismic line CC', conducted with high resolution specifications (higher frequency source, shorter geophone interval, higher recording sampling), confirmed this consideration and described these layers in detail.

Evaluating all these data from BB' and CC', we propose a stratigraphic model from top to bottom with the following layers:

a. Surface sandy silt material from the top to a depth of about 3–4 m.
b. Loose formation probably silty with some gravel and sands or aquifer. The identification of this formation was based mainly on the physical properties of the materials since it seems very loose showing very low s-wave velocity (about 0.4 km/s) and p-wave velocity 1.8 km/s. The estimated Poisson ratio is about 0.47–0.48 indicating the loose and saturation condition of the formation. The layer extends from 4 m to 10–25 m depth along the two profiles. This layer may probably cause liquefaction after the occurrence of a very strong earthquake, so detailed analysis is proposed.
c. The following layer is of denser sedimentation showing higher p-wave velocity (2.2 km/s) and s-wave (0.75 km/s). The sedimentation becomes even denser at depths below 35 m. In addition the high resolution seismic line CC' described a reflector at this depth.
d. The bottom layer is the limestone bedrock. At the end of BB' and the start of CC', the bedrock was detected at the shallower depths so that we can consider a slight uplift at this point. This uplift seems to be connected with the uplift of the bedrock at the long profile (at the offset of 650 m) and the morphology of the hill to the east of the long profile.

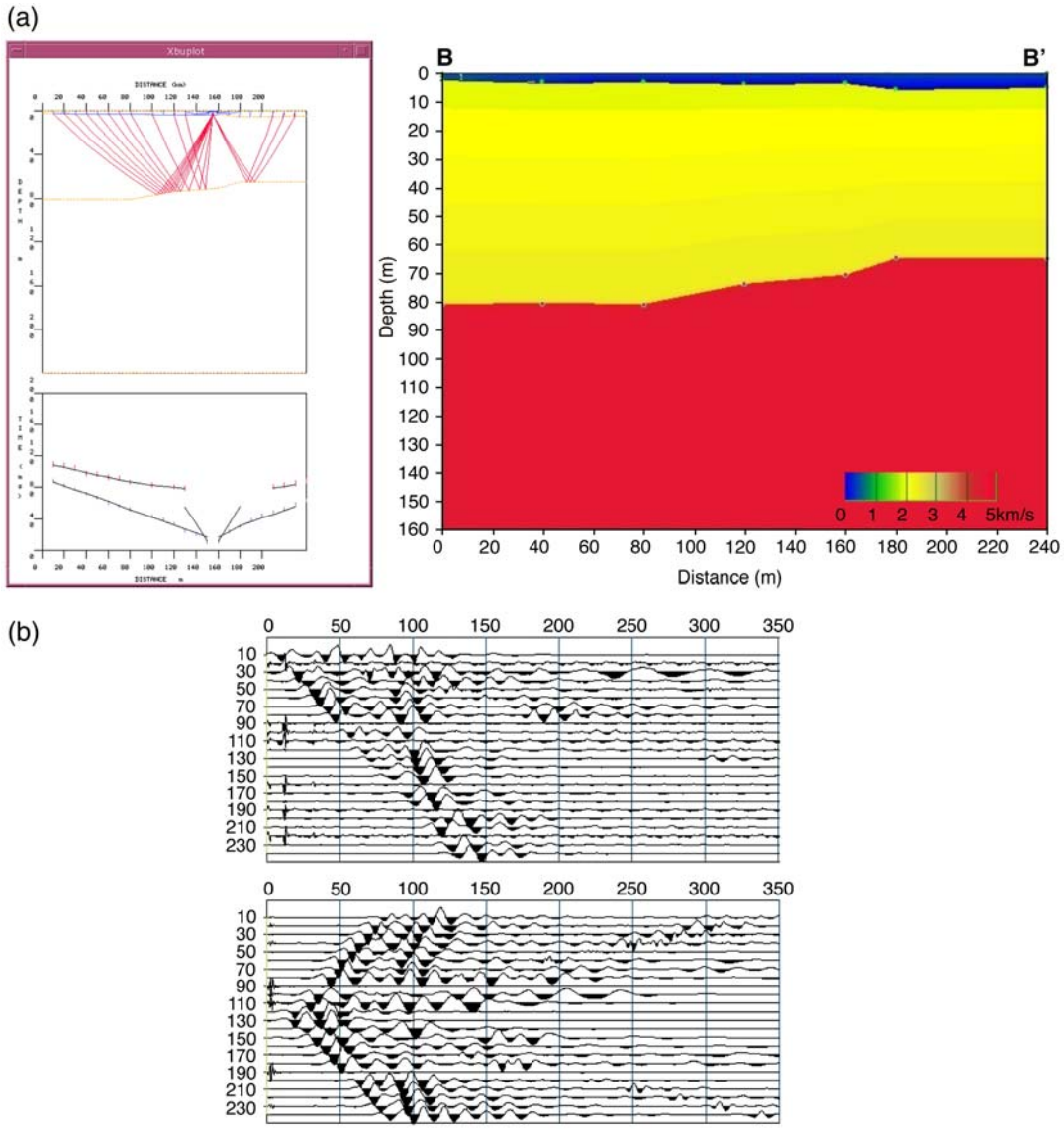

Fig. 8. (a) An example of the processing (on the left) and the final section of BB' seismic line. (b) Examples of the seismic records of BB'. The reflection signal is clear at 0.1 s.

5.3. Lines DD', OO'

The 288 m long profile DD' (see Fig. 3) was conducted near the mountain escarpment, which is related to long-term slip of the Atalanti fault, and at short distance from the coast. The quality of the data was very good for both the refraction and reflection signals (Fig. 9). The results from the seismic tomography and inverse modelling (Fig. 10) indicated that the bedrock was found at 80–90 m depth. In particular, if we consider the second layer with uniform p-wave velocity of about 2.4 km/s the estimated bedrock depth varies from 80 to 85 m. With Zelt and Smith's code (1992) with joint inversion of the reflected and refracted arrivals we used a gradient velocity model (2.3–2.8 km/s) and found the bedrock horizon slightly deeper, about 89 m. We present the processing of the survey in Fig. 11 in order to demonstrate the ability of wide-angle reflections to describe shallow structures.

The first layer (Fig. 10) consists of sand and clay (Vp=1.0 km/s, Vs=0.45 km/s) and reaches a depth of 8 m. The second layer is of dense sedimentation, consisting probably of clay with sand and gravels (Vp=2.4 km/s, Vs=0.9 km/s). The third layer is the

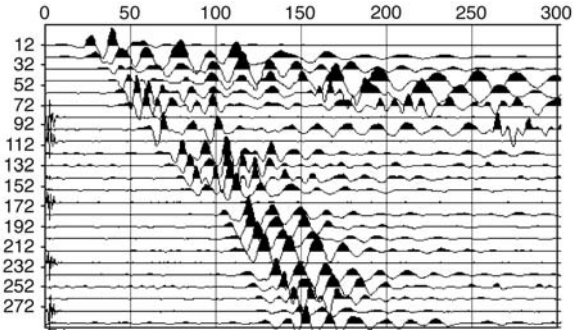

Fig. 9. A record from the seismic profile DD'. The reflection is obvious at about 100 ms.

limestone bedrock with p-wave velocity exceeding 5 km/s.

Although the reflection points of bedrock might not actually be beneath the seismic line (Fig. 15), this result can be very useful in roughly estimating the dip of the fault.

The path of the reflection can be easily estimated from the simple model of Fig. 12. We estimated the dip of the fault to be about 49°. In the calculations we took into account Snell's Law, the distance of the line from the outcrop, the slope of the limestone scarp, the slope of the talus, the relative elevation of line with the geological borders of the talus and the bedrock outcrop. The only accepted precondition is that the fault surface is planar.

Under the line DD' no aquifer was detected since the estimated dynamic Poisson ratio values were 0.37 and 0.42 for the first and the second layer respectively.

At the area of OO' (see Fig. 3) the 1894 earthquakes caused strong liquefaction phenomena. At this site beyond the seismic survey we drilled also a 60 m deep borehole, BH2 (see Fig. 3) and therefore had the ability to correlate seismic velocities with lithology. Fig. 13 shows the correlation between lithology and the s-wave velocity log resulting from MASW. The refraction surveys of P and S waves also showed the respective correlations. Combining all the results we identified the loose second layer (with Vp = 1.26 km/s Vs = 0.14 km/s) as silty gravel of loose deposition and no plasticity. This layer presents a dynamic Poisson ratio of 0.49. All the deeper layers are saturated and their p-wave velocity successively increases from 1.6 to 2.1 km/s. The s-wave

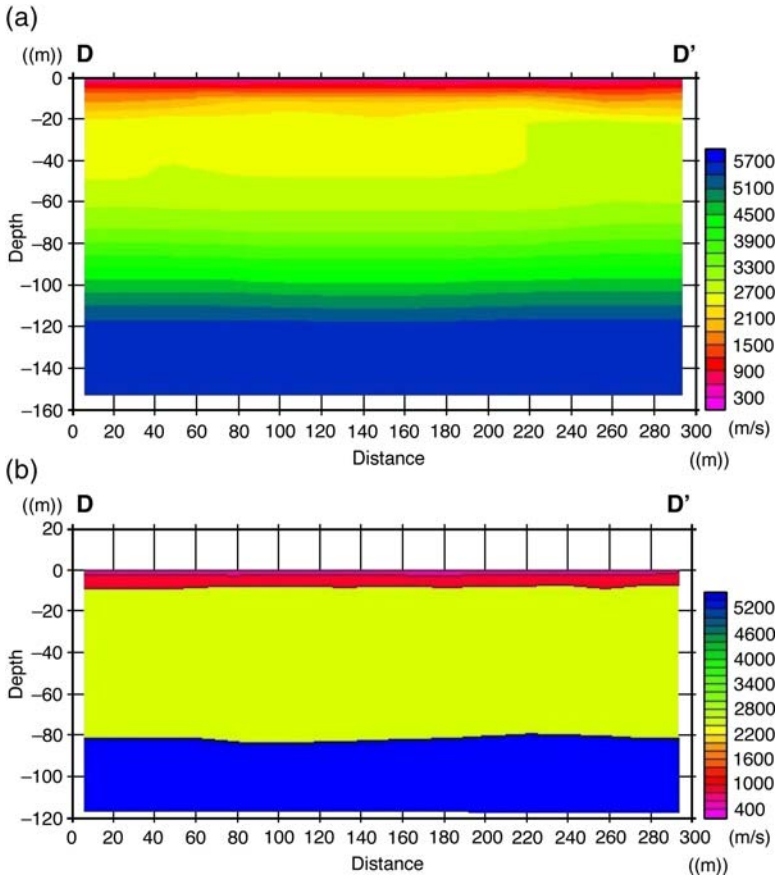

Fig. 10. The model resulting from the refraction tomography (a) and inverse wide-angle modelling (b).

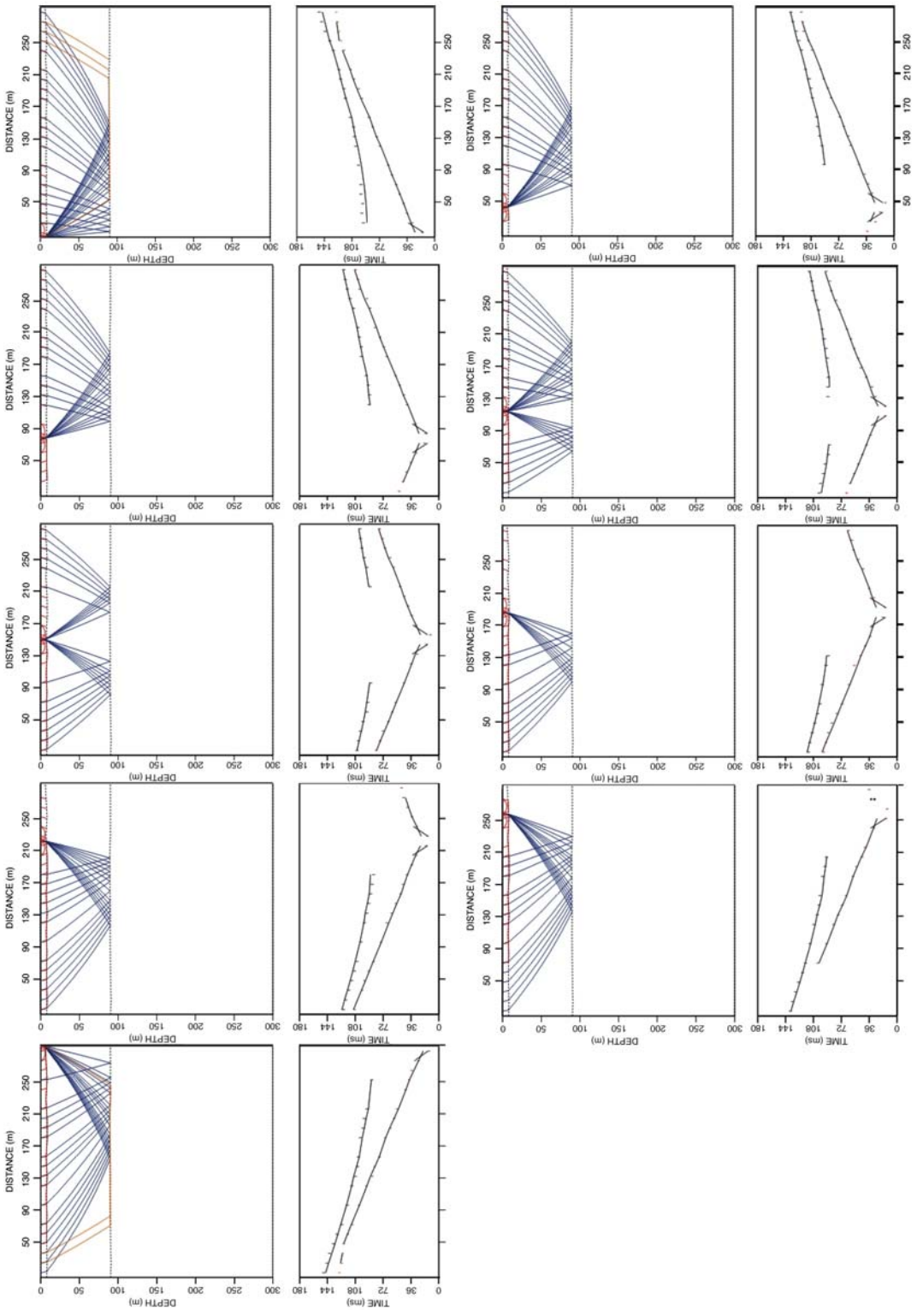

Fig. 11. Ray-tracing for the reflection and refraction arrivals from bedrock in DD'.

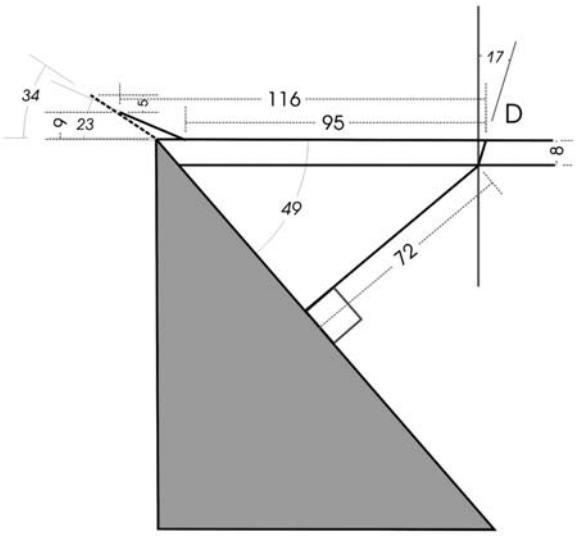

Fig. 12. Vertical section showing the relationship between the seismic line and the inclination of the fault plane. (The orientation of the seismic line is perpendicular to the section and only its front point is seen). The angular values are: 49° is the dip of the Atalanti Fault, 23° is the dip of the scree deposits, and 34° is the slope angle of mountain. The reflection path in the case of the DD' is not perpendicular to the survey plane. The reflection and refraction path is vertical to the fault's plane.

velocity also increases from 0.42 to 0.75 km/s. The deeper formation has a Poisson ratio of 0.42 equal to the value of the second layer in DD', and so it is reasonable to assume that this formation extended up to DD'.

5.4. Lines II', EE', FF', GG', HH'

At the north-western coastal zone of the investigated area, the 1894 earthquakes caused considerable subsidence and detachment of land parts, however a summer house settlement, called "Paliomagaza" (see Fig. 2), has recently been built in this area. Since the limestone is outcropping (near site II' — see Fig. 3) we investigated how the bedrock is dipping to the north by conducting successive profiles II', EE' and FF'. GG' and HH' were carried out close to the houses in order to investigate the quality of the foundation ground.

Profile II' (Fig. 14) revealed that the limestone bedrock is flat and has a smooth apparent dip towards the N315°E profile direction, equal to about 10°.

The results of the processing of the 130 m profile EE' line showed reflectors at 40 m and about 70 m depth. Although these depths are probably apparent too, the depth of the lower horizon is compatible with a normal continuation of the bedrock horizon as described in II'.

The 250 m long profile FF' for the first 40 m is filled with loose, probably silty material. Beneath this layer we found a more compacted layer consisting probably of gravel and sand. Although the seismic profile describes in detail the interface between the silty material with the gravel below, only few seismic records of the line indicate that a deeper reflector exists at about 160 ms. Under the condition of a flat layered model

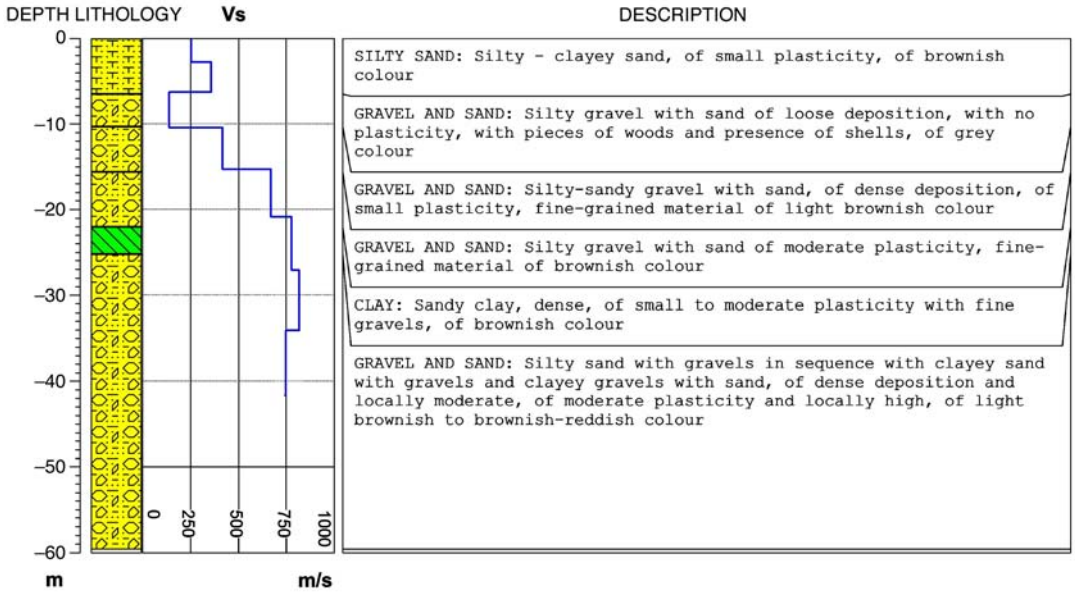

Fig. 13. The results of the borehole BH2 (see Fig. 3 for the location). In the same graph the results of the MASW at the site OO' are shown. The MASW method estimated with accuracy the s-wave velocity of the layers and helped with the layer identification in all the neighbouring profiles.

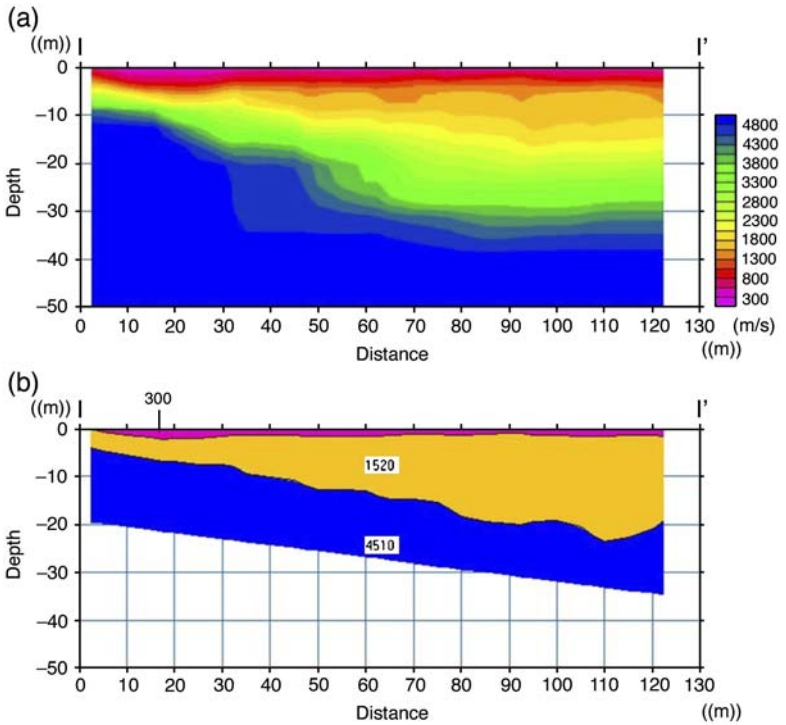

Fig. 14. (a). The results of the refraction tomography at Site II'. (b) The inverse modelling resulted in a 3-layer model. The apparent dip of the bedrock is about 10°.

(Fig. 15) this reflector can be attributed to a horizon 150 m deep.

Besides the information on the silty layer, Profile GG' also provides a good example of how the wide-angle seismic reflection modelling can be fully applicable at shallow depths. This profile showed that the first 40 m consists of loose material with very low s-wave velocity, probably silty sand or aquifer. The processing took into account all the possible phases as primary and multiple reflections from the P and PS mode-converted waves. In Fig. 16 an example is shown from Profile GG', with the modelling of reflected and refracted p-wave arrivals, their multiples and also their PS mode-converted waves.

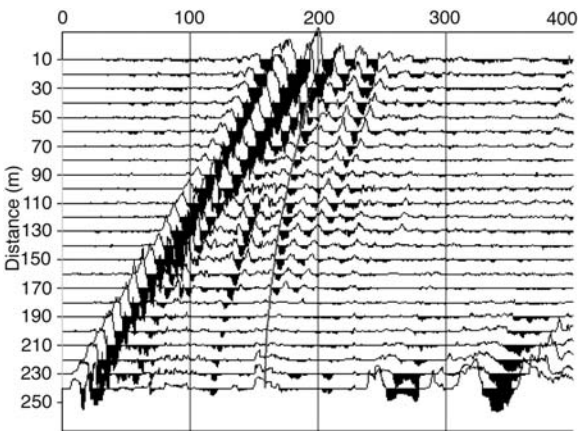

Fig. 15. A velocity filtered record of FF' seismic line. The event at about 160 ms can be attributed to a reflection from the bedrock, and that at about 116 ms is a multiple reflection of this at 58 ms. The event at 58 ms comes from the interface between silty layers and the layer of gravel and sand.

Processing of the mode-converted PS waves showed that the dynamic Poisson ratio of the silty sand layer is close to 0.48, indicative of saturation of the layer.

Although the energy content of the seismic source was high, since the dropping weight was used, no indication of the bedrock reflector was observed.

5.5. Lines KK', LL', MM', NN'

In order to have an overall view of the morphology of the bedrock in this area, as well as a clearer picture of the fault location and geometry, we carried out four seismic lines close to Kyparissi village (Fig. 2). The 288 m long seismic profile KK' (Fig. 3) which was carried out inside the village gave useful information on the depth

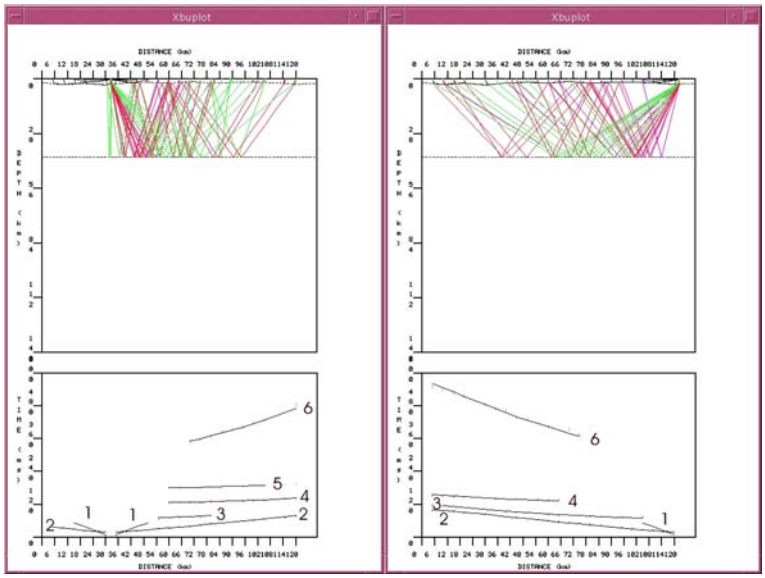

Fig. 16. Example of the processing of the GG' profile, showing the modelling of the arrivals from the direct waves (1), the refractions (2), the primary reflections (3), the multiple reflections (4, 5) and the mode-converted waves (6).

of the bedrock. The accelerated dropping weight provided a high-quality reflection signal, an example of which is given in Fig. 17a. The final model and two examples of the inverse modelling processing are also depicted in Fig. 17b and 17c respectively.

The identification of the layers was based on the estimated velocity values. The limestone bedrock may be the reflector at a depth ranging from 200 to 250 m since at this depth it was the strongest horizon as far as the reflector amplitude is concerned. Over this horizon, there is a consolidated marl layer. Some metres beneath the surface and up to a depth of 100–150 m there are sedimentary deposits of sand and gravel. At about 430 m depth we detected another reflector that can be a side reflection from the fault plane.

Profile LL' (Fig. 18) is located to the east of the beer factory (south of Kyparissi) and close to a scarp that could be related to the Atalanti fault because surface ruptures were observed in 1894 (Skouphos, 1894). However, the profile shows a low dip angle of the bedrock, so it is possible that the scarp seen at the surface represents a southern branch of the main Atalanti fault. Therefore, the location of the main Atalanti fault appears to be further to the north of the profile, i.e. through Kyparissi. In the other two profiles, MM', NN', the bedrock was found at a very shallow depth, up to 10–11 m.

We also tried to trace the Atalanti fault to the east of Tragana by conducting the 288 m long profile RR', but we concluded that the whole profile was located at the hanging wall. The bedrock was detected from only some reflection arrivals and roughly estimated to be at about 160 m depth. This estimation is in agreement with the results of the long profile. However, the RR' profile detected two small normal faults in the sedimentary formations.

6. Discussion

6.1. Tectonic implications of the geophysical data

1. The results from the line AA' which trends north–south show:
   a) the existence of an E–W striking, N-dipping active normal fault off Gaidouronissi Island (see Figs. 3 and 6b — fault F3). The fault is active because our data show low p-wave velocity values (2000–3500 m/s) on its hanging wall compatible with those found inside the Tragana plain, which are basin fill deposits of probable Pliocene age. We estimate a throw of about 300 m for this fault assuming that the bottom strong reflector is the Jurassic limestone outcropping on Gaidouronissi (see Fig. 3),
   b) the Atalanti fault was found beneath the Tragana plain dipping about 45° to the North (Fig. 6b — fault F1). The depth of the basement of the hanging wall was found at 220 m (at a distance 1.75–1.95 km from the coast) consisting of limestone (p-wave velocities up to 4400 m/s).

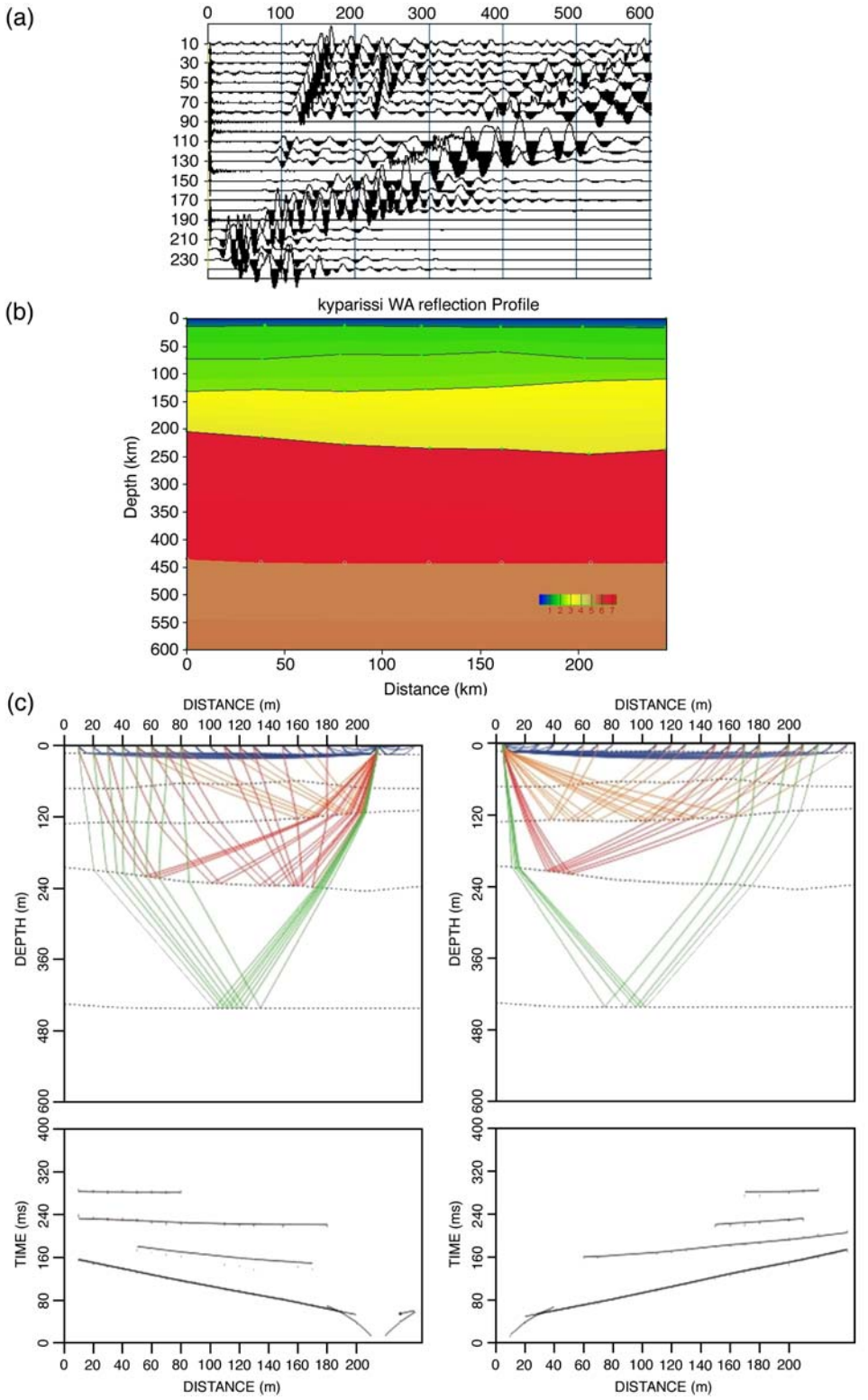

Fig. 17. (a) A seismic record from the KK' profile. The reflection signal is strong and clear, (b) the final model resulting from the modelling, and (c) two examples of the inverse modelling of Line KK'.

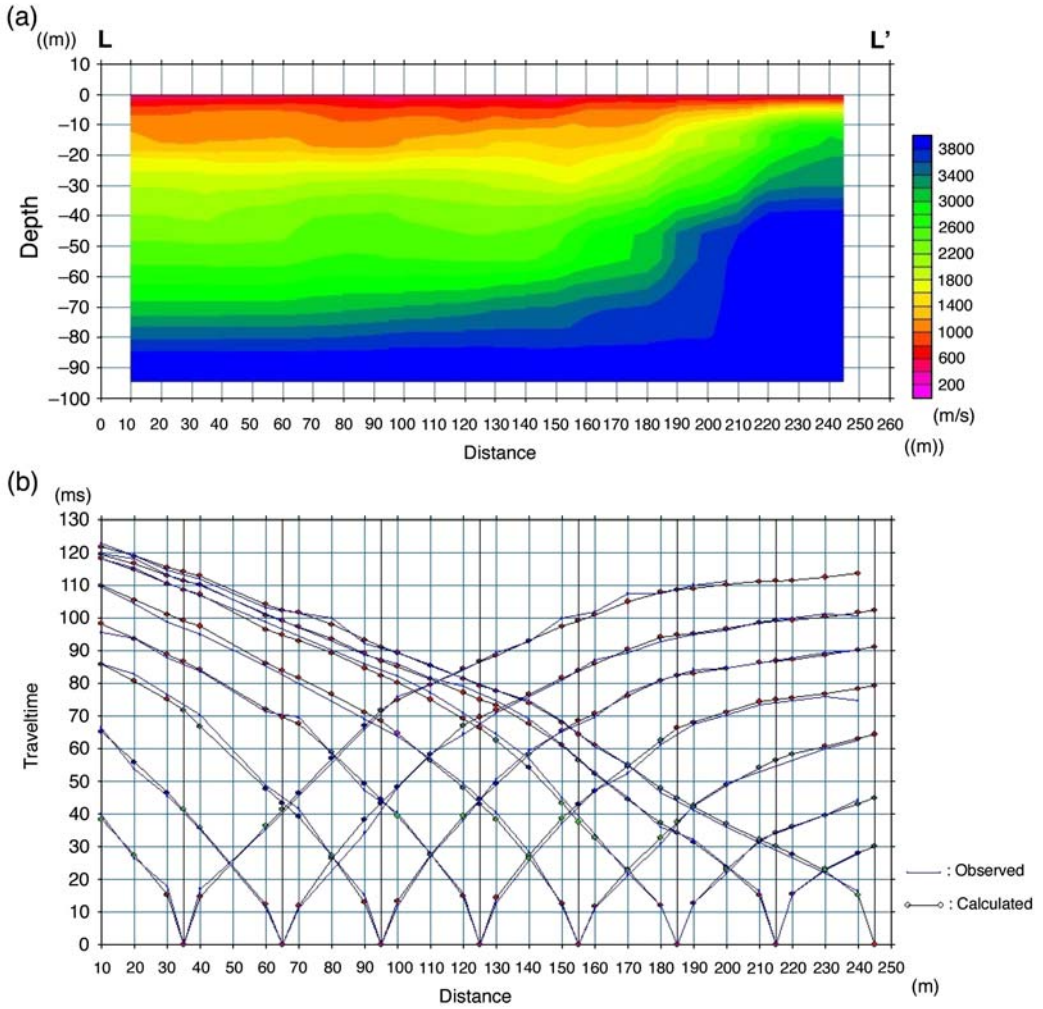

Fig. 18. (a) The refraction tomography section of Line LL'. (b) The observed and the calculated arrivals present a very good fitting.

This structural datum may be correlated with the limestone outcrop south of Tragana, which has an altitude of 262 m. We may use the above observations to estimate cumulative slip along the Atalanti fault as follows: The total throw is about 480 m. Assuming (a) pure dip-slip motion along a fault plane dipping 45° and (b) pre-rift flat morphology and applying the Pythagoras theorem we obtain slip = [Square root (throw^2 + heave^2)] = 680 m.

c) south of Tragana town the shallowest position of the limestone basement was found 2.2 km far from the coast. This position coincides with the appearance of the mountain front on the Earth's surface which in turn confirms that the fault plane runs E–W along the base of the mountain front. Our results also include the imaging of two other normal faults, synthetic to the Atalanti Fault: i) Fault F4 off Gaidouronissi and ii) Fault F2 off Mitrou. The existence of the latter is confirmed by the occurrence of diabase (basement) on the north coast of Mitrou island (Fig. 3) which indicates a relative uplift of the basement. Fault F2 strikes N288°E and dips to the North with a high angle. The estimated throw is about 100 m and its length at about 1500 m (Fig. 3).

2. Line DD' trends parallel to the Atalanti Fault trace (WNW–ESE; Fig. 3) at a distance of about 108 m (Fig. 12). The basement that was detected at depth was the fault plane itself (see Fig. 12) due to side reflection of the P-waves. This geometry between the basement interface and the distance to the mountain front on the Earth's surface suggests that the Atalanti fault also dips to the North with a moderate angle of 49°.

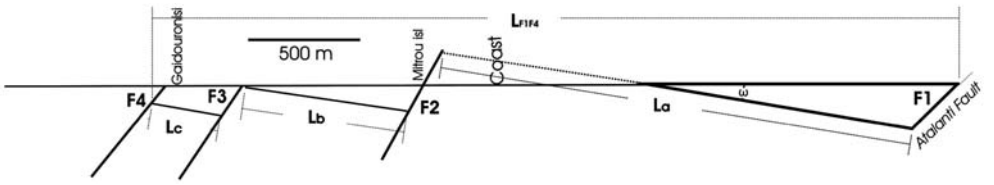

Fig. 19. Structural cross-section along Line AA' showing location of active faults and tilt of basement due to longitudinal extension. See text for discussion.

3. In line KK' the depth of the limestone bedrock was estimated to be 200–250 m. The profile was conducted at about 650 m north of the fault scarp (Fig. 3). If the fault plane, with a dip of 45°, was the interface between the bedrock and the Neogene sediments, below the seismic line, the profile should have estimated depth of the bedrock to be about 470 m. By contrast, we estimated depth up to 200–250 m, thus this result can be used to estimate the minimum throw of the Atalanti Fault at this locality. The height of the footwall in this area is about 230 m (Kourkouras hill, HAGS, 1971) so a minimum throw is about 430–480 m assuming flat, pre-rift topography. The deeper reflections must originate from the fault plane itself that probably dips with an angle of about 45° to the North. This reflector seems to be the deeper horizon since the wave path from the seismic source to the fault plane and finally to the receivers passes through the limestone.

6.2. The geometry, slip distribution and finite slip of the Atalanti Fault

Our results may be used to study the long-term strain distribution along the strike of the Atalanti Fault. First, our seismic profiles point to a constant, northward dip of the fault of about 45° for a distance of at least 8 km (Fig. 3). This dip is characteristic of a mature normal fault that accumulates slip for a period of 2–3 My. Second, our data show a simple basin stratigraphy with a lacustrine sedimentation at the base (Pliocene) becoming more fluvial towards the top of the column (Upper Quaternary). Third, the Atalanti Fault was found to comprise one segment in our study area, in agreement with the fault models of Ganas et al. (1998) and Roberts and Ganas (2000). The fault throw near Tragana is almost 480 m which is indicative of the existence of a fault bend in this area and not a right step between two segments of a fault zone. In the latter case the fault throw near Tragana should be one order of magnitude smaller. A mimimum throw of 430–480 m is estimated for the region of Kyparissi (profile KK'), which suggests a similar slip history for these two portions of the fault plane. Fourth, the Atalanti fault is the main structure accommodating extension in this area of the Gulf of Evia rift. The other major structure is an active normal fault off Gaidouronissi (Fig. 3), which maintains a synthetic geometry to Atalanti with a length of at least 6.5 km. Finally, throughout the study area there is no evidence for any cross-faults in the basement or for any NE–SW faulting inside the hanging wall.

6.3. Hanging wall structure and crustal extension estimates

From the data of the line AA′ we observe that the tectonics of the Atalanti hanging wall are represented by fault block rotation about a horizontal axis with all faults approximately striking E–W and dipping to the North at 45–47°. We assume plain strain with no extension horizontally along the rotational axis. Our data do not permit the introduction of a reference horizon at depth, however, on the basis of seismological data for large earthquakes in central Greece, we may accept the reference datum to be at 12–15 km. These observations result in a typical, domino-type of fault tectonics where planar, sub-parallel normal faults divide the extending crust into rigid (domino) blocks. We have no data to propose either a basal detachment on this depth or continuation of the faults into the lower crust as ductile shear zones.

The geophysical data provide useful information to roughly estimate the amount of crustal extension along the N–S direction in the Atalanti area. The stretching factor β is equal to the width of the structure (faulted area) divided by the original block length (Fig. 19), i.e. $\beta = L_{F1F4}/\mathrm{La}+\mathrm{Lb}+\mathrm{Lc}$ or $\beta = 3688\ \mathrm{m}/(2172\ \mathrm{m}+747\ \mathrm{m}+316\ \mathrm{m})$ or $\beta = 1.14$.

A second way to estimate β is to use the angular relationships of the domino array. We accept that the maximum compressive stress $\sigma 1$ is vertical and using a Navier–Coulomb rheology the dip of the faults at surface (θ) is given by $\theta = 90° - (45° - \varphi/2)$ where φ is the angle of friction of the crustal material. φ ranges between 30°–35° for upper crustal rocks. Therefore

the initial fault dip would be 60°–62.5°. The amount of the horizontal extension can be directly calculated using the following equation (Davison, 1989): $\beta = \sin\theta / \sin(\theta - \omega)$, where θ is the initial fault dip and ω is the final, pre-rift basement dip, assuming that the basement was initially horizontal before faulting. From section we observe that $\omega = 10°$ so $\beta = \sin 60 / \sin 50$ or $\beta = 1.13$. This estimate assumes that the blocks behave in a totally rigid manner so that β is constant at all levels in the crust. Thus, both methods supply almost identical values of β.

The comparable thickness of the hanging wall sediments, the uniform dip of the basement and the final fault dip angles suggest that all four faults in the array were initiated at about the same time and moved simultaneously. The finite slip of the Atalanti fault is the larger of the array so this is the master fault of the sequence.

7. Conclusions

The shallow seismic surveys can considerably aid the structural investigations in areas of active faults. Nevertheless it is essential for the interpretation of the results to take account of geomorphological and geological data, so the acquired information can contribute to the improvement of the structural models.

Seismic wide-angle modelling can be a valuable tool in the shallow geophysics but needs extra care on discriminating and identifying the reflection signal.

We found an almost constant, northward dip of the Atalanti Fault of about 45–49° for a distance of at least 8 km (Fig. 3).

Our data show a simple basin stratigraphy with a lacustrine sedimentation at the base (Pliocene) becoming more fluvial towards the top of the column (Upper Quaternary).

The Atalanti Fault was found to comprise one segment in our study area.

The Atalanti fault is the main structure accommodating extension in this area of the Gulf of Evia rift. A second active normal fault exists offshore at Gaidouronissi (Fig. 3) in synthetic geometry to Atalanti with a length of at least 6.5 km.

Upper crustal extension due to the Atalanti domino array is estimated at 13–14%.

In our seismic lines we found no evidence for any cross-faults in the basement or for any NE–SW faulting in the hanging wall.

In a large part of the coastal zone, mostly at the northern, the Poisson ratio was found at values about 0.48–0.49, indicative of saturation in loose sediments. Such areas need to be investigated for their liquefaction potential as they are composed of unconsolidated, sandy and silty material.

Acknowledgments

We thank the General Secretariat for Research and Technology in the Ministry of Development for funding the project “AMPHITRITE”, the Director of the Institute of Geodynamics Dr G. Stavrakakis who provided us with vehicles and many parts of the equipment used, the Major of Atalanti, Mr L. Brekoulakis, and Mr G. Berdos for their assistance, and the Fire Brigade of Atalanti. We especially thank the Director Officer, Mr Sifakis, for his considerable help in our survey since he provided us with working and storage rooms. We also thank the Coastal Police of Atalanti who provided us space in their small marina for our vessel.

Special thanks to Dr Elias Gerolymatos, who joined us in a geological field trip and considerably helped us with his comments and his ideas about the tectonic regime of the Atalanti faulted zone.

We would also like to thank the people who joined us in the fieldwork: Dr D. Illinski, Mr G. Michaletos, Mr Th. Vourakis, Mr M. Papanikolaou, Mr E. Papantoniou, Mr N. Ziabko, Mr A. Alabyev, Mr S. Liakopoulos, Mr I. Peponakis and Mr M. Arvanitis.

Special thanks to the directors of Geoskopio, Ch. Alexiadou and A. Panagopoulos, for their considerable contribution to the geological survey of the area, in conducting and interpreting the boreholes as well as the topographic survey for the project.

We would finally like to thank Dr R. E. Jones, University of Glasgow, for reviewing the paper.

References

Ambraseys, N.N., Jackson, J.A., 1990. Seismicity and associated strain of central Greece between 1890 and 1988. Geophys. J. Int. 101, 663–708.

Buck, V., Stewart, I., 2000. A critical reappraisal of the classical texts and archaeological evidence for earthquakes in the Atalanti region, central mainland Greece. In: McGuire, W.G., Griffiths, D.R., Hancock, P.L., Stewart, I.S. (Eds.), The Archaeology of Geological Catastrophes. Geological Society, London, Special Publications, vol. 171, pp. 33–44.

Cundy, A.B., Kortekaas, S., Dewez, T., Stewart, I., Croudace, W., Maroukian, H., Papanastassiou, D., Gaki-Papanastassiou, P., Pavlopoulos, K., Dawson, A., 2000. Coastal impacts of the 1894 Gulf of Atalanti earthquakes, central Greece. Mar. Geol. Spec. Publ. 170, 3–26.

Davison, I., 1989. Extensional domino fault tectonics: kinematics and geometrical constraints. Ann. Tecton. 3, 12–24.

Ditmar, P., Penopp, J., Rainer, K., Makris, J., 1999. Interpretation of shallow refraction seismic data by reflection/refraction tomography. Geophys. Prospect. 47, 871–901.

Gabriels, P., Snieder, R., Nolet, G., 1987. In situ measurements of shear-wave velocity in sediments with higher-mode Rayleigh waves. Geophys. Prospect. 35, 187–196.

Ganas, A., Papoulia, I., 2000. High-resolution digital mapping of the seismic hazard within the Gulf of Evia rift, Eastern Central Greece using normal fault segments as line sources. Nat. Hazards 22, 203–223.

Ganas, A., Roberts, G.P., Memou, T., 1998. Segment boundaries, the 1894 ruptures and strain patterns along the Atalanti fault, central Greece. J. Geodyn. 26, 461–486.

HAGS (1971) (Hellenic Army Geographical Service). Livanates Map Sheet, 1:50000. Athens.

Hayashi, K., Takahashi, T., 1997. High resolution seismic refraction survey using surface and borehole data for site characterization of rocks. Proceedings of International Workshop, ISRM Symposium: NYRocks'97, Application of Geophysics to Rock Engineering, pp. 17–24.

IGME, 1965. Geological map of Greece. Sheet Atalanti. Scale 1:50000, Athens.

Lin, C.P., Chang, C.C., Chang, T.S., 2004. The use of MASW method in the assessment of soil liquefaction potential. Soil Dyn. Earthqu. Eng. 24, 689–698.

Makris, J., Moeller, L., 1990. An ocean bottom seismograph for general use. Technical requirements and applications. In: Hoefeld, J., Mitzlaff, A., Polomsky, S. (Eds.), Proceedings of Symposium "Europe and the Sea", Hamburg.

McMechan, G.A., Yedlin, M.J., 1981. Analysis of dispersive waves by wave field transformation. Geophysics 46, 869–874.

Mitsopoulos, K., 1895. The Lokris Mega-Earthquake. (in Greek), 40 pp. Athens.

Morozov, I.B., Levander, A., 2002. Depth image focusing in traveltime map based wide-angle migration. Geophysics 67, 1903–1912.

Pantosti, D., De Martini, P.M., Papanastassiou, D., Palyvos, N., Lemeille, F., Stavrakakis, G., 2001. A reappraisal of the 1894 Atalanti earthquake surface ruptures, Central Greece. Bull. Seismol. Soc. Am. 91, 760–780.

Pantosti, D., De Martini, P.M., Papanastassiou, D., Lemeille, F., Palyvos, N., Stavrakakis, G., 2004. Paleoseismological trenching across the Atalanti Fault (Central Greece): evidence for the Ancestors of the 1894. Earthquake during the Middle Age and Roman Times. Bull. Seismol. Soc. Am. 94, 531–549.

Papaioannou, I., Papadopoulos, G.A., Pavlides, S., 2004. The Earthquake of 426bc, Gulf revisited: amalgamation of two different strong earthquake events? In: Evoikos, N. (Ed.), Proceedings of the 10th International Congress, Thessaloniki, April 2004. Bulletin of the Geological Society of Greece, vol. 36, pp. 1477–1481.

Park, C.B., Miller, R.D., Xia, J., 1999. Multi-channel analysis of surface waves (MASW). Geophysics 64, 800–808.

Pavlides, S.B., Valkaniotis, S., Ganas, A., Keramydas, D., Sboras, S., 2004. The active fault of Atalanti — Re-evaluation with new geological data. Bull. Geol. Soc. Greece 36, 1560–1567 (in Greek).

Roberts, G.P., Ganas, A., 2000. Fault–slip directions in central and southern Greece measured from striated and corrugated fault planes: comparison with focal mechanism and geodetic data. J. Geophys. Res. 105, 23443–23462.

Roberts, S., Jackson, J., 1991. Active normal faulting in central Greece: an overview. In: Roberts, A., Yielding, M., Freeman, G. (Eds.), The Geometry of Normal Faults. Geol. Sot. Sp. Publ., vol. 56, pp. 125–142.

Rondoyianni-Tsiambaou, Th., 1984. Etude Néotectonique des rivages occidentaux du canal d'Atalanti (Grèce Centrale), 200 p. Doctoral Dissertation, Université: de Paris Sud.

Skouphos, T., 1894. Die swei grossen Erdbeben in Lokris am 8/20 und 15/27 April 1894. Zeitschrift Ges. Erdkd. Berl. 24, 409–474 (in German).

Xia, J., Miller, R.D., Park, C.B., 1999. Estimation of near-surface shear-wave velocity by inversion of Rayleigh waves. Geophysics 64, 691–700.

Zelt, C.A., Forsyth, D.A., 1994. Modeling wide-angle seismic data for crustal structure: southeastern Greenville province. J. Geophys. Res. 99, 11687–11704.

Zelt, C.A., Smith, R.B., 1992. Seismic traveltime inversion for 2-D crustal velocity structure. Geophys. J. Int. 108, 16–34.